In Situ Al-TiC Composites Fabricated by Self-propagating High-Temperature Reaction: Insights on Reaction Pathways and Their Microstructural Signatures



C.W. REESE, A. GLADSTEIN, J.M. FEDORS, V. DE ANDRADE, B. MISHRA, A.J. SHAHANI, and A.I. TAUB

In this study, we have analyzed the formation mechanisms and processing-microstructure relationships for Al/TiC metal matrix nanocomposites produced in situ via thermite-assisted (e.g., CuO) self-propagating high-temperature synthesis (SHS). Al/TiC composites were created by reacting Al-Ti-C-CuO pellets in an Al melt using a wide variety of processing conditions (e.g., precursor powder amounts, bulk melt temperature, precursor powder size, pellet packing method). As-cast composites were visualized using both 2D (SEM) and 3D (TXM) microscopy techniques, to study TiC particle and secondary precipitate (e.g., Al₃Ti) characteristics at the nanoscale. SHS-produced samples reveal complex microstructures consisting of individual and clustered TiC particles, elongated Al₃Ti intermetallics, and C-rich regions surrounded by TiC. Based on a thermodynamic analysis and our microstructural observations, we propose three dominant TiC formation pathways, each resulting in a distinct microstructural signature. Finally, we utilize multivariate statistics (canonical correlations) on the full breadth of imaging data to infer the dominant processing variables (i.e., amount of CuO and C) that most strongly influence TiC particle characteristics and the final composite microstructure. We also discuss how the dominant processing variables relate to the proposed formation pathways and how they may inform the rational design of future composites produced via thermite-assisted SHS.

https://doi.org/10.1007/s11661-020-05786-1 © The Minerals, Metals & Materials Society and ASM International 2020

I. INTRODUCTION

IN recent years, much attention has been given to the concept of light weighting, particularly in the automotive and aerospace industries, in order to meet stringent guidelines for fuel economy. This trend toward light weighting has led to an increased use of and interest in aluminum alloys due to their high strength-to-weight ratio, low cost, and ability to be work- or precipitation-hardened. [1–5] However, aluminum alloys

C.W. REESE, A. GLADSTEIN, and A.J. SHAHANI are with the Materials Science & Engineering, University of Michigan, Ann Arbor, MI 48109. J.M. FEDORS is with the Materials Science & Engineering, Worcester Polytechnic Institute, Worcester, MA 01609. V. DE ANDRADE is with the Advanced Photon Source, Argonne National Laboratory, Argonne, IL 60439. B. MISHRA is with the Materials Science & Engineering, Worcester Polytechnic Institute and also with the Mechanical Engineering, Worcester Polytechnic Institute, Worcester, MA 01609. A.I. TAUB is with the Materials Science & Engineering, University of Michigan and also with the Mechanical Engineering, University of Michigan, Ann Arbor, MI 48104. Contact e-mail: alantaub@umich.edu

Manuscript submitted October 14, 2019. Article published online May 8, 2020

commonly suffer from poor mechanical properties at elevated temperature, making their use in many industrial applications limited. Metal matrix nanocomposites (MMNCs) offer a potential pathway toward improving the high-temperature performance of Al-based materials via the incorporation of small amounts of refractory reinforcement particles. MMNCs are typically manufactured via ex situ processing, wherein precursor particles are added to a melt during processing. [6] However, ex situ MMNCs can suffer from the high precursor cost, poor wetting between matrix/reinforcement, and contamination of reinforcement powders.[7] Alternatively, particles can also be created directly in the melt via in situ reactions during processing. Previous work has demonstrated the possibility of particle formation through direct reaction between the constituent elements (e.g., solid–liquid reaction^[8,9] or liquid–gas reaction^[10,11]), as well as through solid-state diffusion-mediated reactions between compounds and individual elements (e.g., displacement reaction^[12–18]). In situ MMNCs exhibit reduced particle agglomeration and stronger particle-matrix interfacial bonding. [19,20]

Of the *in situ* methods, the self-propagating high-temperature synthesis (SHS) approach has proven to be

attractive for its ability to fabricate MMNCs in a wide variety of material systems and its potential compatibility with existing commercial equipment. A very promising approach utilizes a small amount of thermite (2.7 mol pct CuO) allowing for the SHS processing of TiC/Al MMNCs at relatively low bulk temperatures (750 °C to 920 °C). [9,21] However, the underlying mechanisms of the particle formation are not well understood which limits the ability to optimize the process for large-scale production. The SHS reaction pathways for TiC formation have been theorized to be complex and several different direct and indirect mechanisms have been hypothesized, each impacting the final microstructure in different ways. [9,21–24]

Our contribution is aimed at answering two main questions: First, what are the governing mechanisms of particle formation? Secondly, how are the reaction mechanisms impacted by the processing variables? To this end, we present an integrated approach to understanding the production of in situ TiC/Al MMNCs via SHS. Focusing on the CuO-assisted method, we analyze a variety of microstructures from different processing conditions using a combination of SEM and 3D transmission X-ray microscopy (TXM) to elucidate the TiC and secondary phase formation mechanisms. To link these microstructural observations to the processing variables in a quantitative manner, we conduct a canonical correlation analysis (CCA). This multivariate statistical technique sheds light on the processing parameters that are maximally correlated with the agglomeration and dispersion of the TiC particles, among other microstructural descriptors.

II. EXPERIMENTAL METHODS

A. SHS Experiments

In situ Al-TiC composites were prepared at Worcester Polytechnic Institute (Worcester, MA) via a modified SHS process developed by Cho et al., wherein pellets containing various ratios of raw elemental powders (Al, Ti, C) and copper thermite (CuO) are directly reacted in an Al melt. [9] In this study, several processing parameters were varied as shown in Table I.

To create the pellets, powders of Al ($\sim 30 \mu m$, 99.5 pct purity), Ti (~ 20 or $\sim 44 \mu m$, 99.7 pct purity), C (9 μm , 99 pct purity), and CuO ($< 10 \mu m$, 98 pct, purity) were mixed in composition ratios of 1.5 mol Al, 1 mol Ti, 1 mol C, and 0.1 mol CuO (with "high" C and CuO compositions corresponding to 1.1 mol and 0.155 mol. respectively, see Table I). Two different mixing methods were used: in the first, Al, Ti, and C powders were ball milled together for 24 hours and then combined with CuO via manual mechanical mixing (to avoid reaction inside the ball mill); and in the other, Al, Ti, C, and CuO were thoroughly mixed via resonant acoustic mixing (RAM). The powder mixture was subsequently pressed into a 30 mm die at 200 MPa to create pressed pellets (~ 20 g per packed pellet), or loosely packed and wrapped in Al-foil (~ 2.4 g per loose pellet, ~ 15 mm diameter). All pellets were pre-heated in a resistance furnace at 373 K (100 °C) for 2 hours prior to each SHS experiment, in order to dry the powders and bake off organic contaminants.

Approximately 500 g of Al ingot (99.99 pct purity) was melted in an induction furnace and pellets were inserted and pushed beneath the surface of the melt using a BN-coated submersion tool (constructed of a flat meshed steel plate and handle). The average bulk processing temperature during each experiment ranged from 1043 K to 1133 K (770 °C to 860 °C). Pellet additions in the melt were staggered by ~ 1 to 2 minutes to allow for the temperature to settle between each pellet. The specific number of pellets added in each batch varied depending on the target reinforcement volume percentages of 10 or 2 vol pct TiC, which corresponded to raw powder/melt mass ratios $(r_{p/m})$ of approximately 0.32 and 0.07 respectively. The $r_{\rm p/m}$ ratios were calculated assuming approximately 100 pct conversion of Ti and C. After pellet addition was completed, all batches were manually stirred and subsequently cast into molds at room temperature then allowed to solidify in ambient conditions.

B. Characterization Techniques

Metallographic specimens for SEM imaging were prepared at The University of Michigan (Ann Arbor, MI) by sectioning as-cast ingots and using standard

Table I	Summary	Table of	Experimental	Conditions	Varied	Retween	SHS	Processing	Ratches
i abie i.	Summary	I able of	Experimentar	Colluluous	v ai ieu	Detween	SHS	riocessing	Datches

Sample ID	C Amount, n_C (mol)	CuO Amount, n_{CuO} (mol)	Ti Size, d _{Ti} (μm)	Pellet Packing Method	Powder Mixing Method (—)	Powder/Melt Ratio, $r_{p/m}$ (g/g Al)	Process Temperature, T_{proc} (°C)
1	1	0.1	44	pressed	ball mill + mechanical mix	0.32	842
2	1	0.1	44	pressed	resonant acoustic mix	0.32	860
3	1.1	0.155	44	pressed	resonant acoustic mix	0.32	838
4	1.1	0.1	44	pressed	resonant acoustic mix	0.32	851
5	1.1	0.155	44	pressed	resonant acoustic mix	0.32	843
6	1.1	0.1	44	pressed	ball mill + mechanical mix	0.32	840
7	1.1	0.155	20	pressed	ball mill + mechanical mix	0.32	823
8	1.1	0.155	20	loose	ball mill + mechanical mix	0.07	780
9	1.1	0.155	20	pressed	ball mill + mechanical mix	0.07	770

polishing procedures with a 1 μ m diamond-suspension finishing step. Bulk microstructural characterization was performed using a Tescan MIRA3 field emission gun (FEG) SEM operating in backscatter electron (BSE) mode at 15 kV and a beam intensity of 12 to 15, while an integrated EDAX energy-dispersive spectroscopy (EDS) system was utilized for chemical identification of particles and secondary precipitates. One hundred and eighty-four images across 18 samples were analyzed in order to provide statistically significant correlations (vide infra Section IV).

The cast samples were also visualized in 3D at nanoscale resolution. Micropillar specimens for TXM characterization were prepared (at The University of Michigan) by taking as-cast ingots and cutting out 1 mm diameter rods (10 to 15 mm in length) via electrical discharge machining (EDM). Rods were subsequently sharpened on one end to approximately 100 μm diameter tips via electropolishing in a solution of 25 vol pct NHO₃ and 75 vol pct CH₃OH at 10 V for bulk material removal and a final polish at 5 to 7.5 V to minimize surface roughness and better control taper. Electropolished tips were shaped into final pillars 40 μ m in diameter and 80 to 100 μ m in height using a FEI Nova 200 Nanolab SEM/FIB equipped with a Ga+ ion beam. A FIB accelerating voltage of 30 keV was used in conjunction with various milling currents, starting with 20 nA for coarse milling and stepping down to 5 and 1 nA to minimize taper and surface roughness.

Absorption full-field hard X-ray nanotomography experiments were conducted via TXM at Sector 32-ID at the Advanced Photon Source in Argonne National Laboratory (Argonne, IL). [25] The un-milled end of each sample was clamped to a stainless steel needle to ensure correct micropillar height in the TXM, and samples were subsequently placed on a high precision air-bearing rotary stage capable of 360 deg rotation. A monochromatic X-ray beam operating at 8 keV was focused onto the samples using a monocapillary condenser and a Fresnel zone plate with 50 nm outermost-zone-width served as an objective lens to magnify the images. Projections were acquired using a detector assembly comprising a LuAG scintillator, a Mitutoyo long working distance objective lens, and a CCD. A more detailed description of the TXM setup is available elsewhere. [25,26] Using this configuration, a spatial resolution of 50 nm for a pixel size of 22.3 nm with a field-of-view of 2448 × 2048 pixels (or approximately 54 \times 45 μ m²) on the detector plane was achieved. For each scan, projections were taken at 0.15 deg angular increments from 0 to 180 deg with an exposure time of 1 or 0.5 seconds (contrast between sample elements was large enough that there was minimal difference between exposure times). In total, we captured 16 scans (tomograms) from 9 different samples via TXM to augment our SEM observations (Section IV).

C. Data Processing and Visualization Methods

SEM micrographs were adjusted to maximize contrast using ImageJ software prior to analysis. A representative micrograph after contrast adjustment is shown in

Figure 1(a). The differences in backscattering contrast easily reveal the Al₃Ti intermetallic precipitates (medium gray) and TiC particles (bright) against the Al matrix (dark). Segmentation or partitioning of phases into different classes and additional post-processing were carried out using the Image Processing toolbox in MATLAB 2018b. In general, the data processing workflow consisted of multi-level thresholding followed by median filtering to reduce background noise. From the segmented and processed images, we calculated the particle (and intermetallic) areas (and hence, effective particle diameters) based on the sizes of individual connected components. The spacing between centroids of connected components (corresponding to the interparticle distance) was done via k-nearest neighbors algorithm.[27-29]

The TXM projection data was reconstructed into 3D using TomoPy, a Python-based open source framework for tomographic data processing. [30] Projections were first normalized using dark- and white-field images and subsequently the data were reconstructed via the Gridrec algorithm with Parzen filtering. [31,32] A representative reconstruction slice along the axis of rotation is shown in Figure 1(b), where the Al matrix (dark gray), Al₃Ti (medium gray), and TiC (bright) are easily distinguishable due to differences in absorption contrast. The grayscale intensities of the individual slices were normalized using the Beer-Lambert law to account for small differences in slice diameter. Subsequently, the 2D slices were segmented using the same approach as for the SEM images. The segmented 2D slices were combined into a 3D volume and post-processed using the same methods as for the SEM images (i.e. median filtering, connected component labeling, and a k-nearest neighbor search). Interfaces between the phases were meshed in 3D to facilitate 3D visualization. A representative mesh is shown in Figure 1(c), with the TiC colored in red and Al₃Ti intermetallics shown in green. A video capture 3D rotation of the mesh is shown in Supplementary Vid. S-1 (refer to electronic supplementary material).

III. RESULTS AND DISCUSSION

A. Microstructural Observations

The observed microstructures consisted of sub-micrometer TiC particles, with small amounts of Al₃Ti and C-rich regions containing unreacted carbon. Micrographs of representative Al₃Ti, C-rich regions, and TiC particles and their corresponding EDS spectra are shown in Figures 2(a) through (c). It is worth noting that a small amount of Al₂O₃ (not shown here) was also observed in the bulk. Since this is a byproduct of the reduction of CuO by liquid Al during thermite reaction^[33–35] and not directly related to the Al-Ti-C system under investigation, we do not focus on the Al₂O₃ phase hereafter.

The Al₃Ti precipitates (Figures 1 and 2(a)) exhibit an elongated and faceted structure with dimensions approximately 10 to 40 μ m long and 5 to 10 μ m wide.

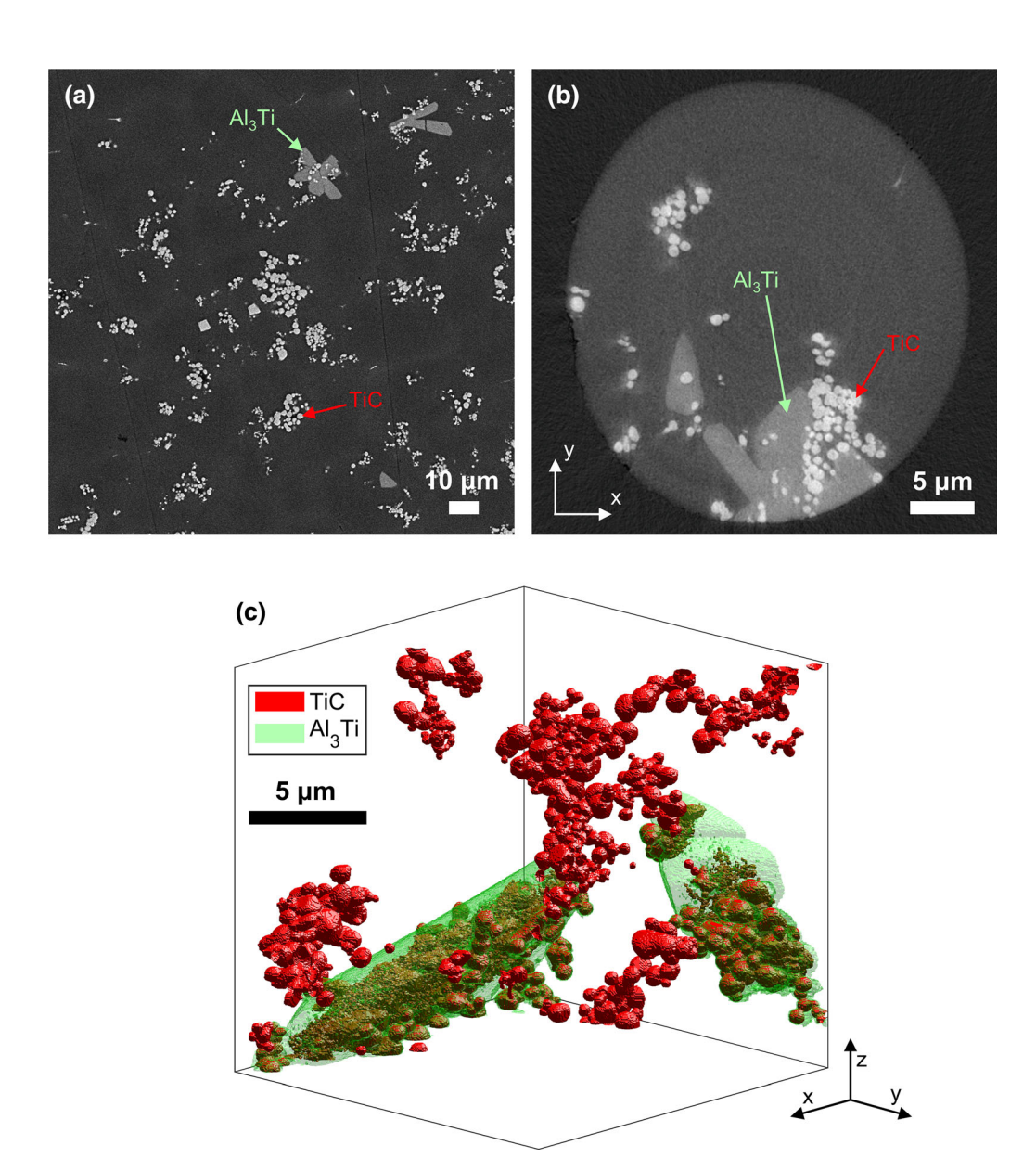


Fig. 1—Microstructural observations: (a) Representative contrast-adjusted SEM micrograph used for image analysis of particles and secondary phases. Both TiC and Al₃Ti intermetallics are present. (b) Representative reconstructed slice (taken along the tomographic axis-of-rotation, \hat{z}) of a micropillar showing both TiC and Al₃Ti phases. The round slice shape corresponds to the diameter of the micropillar, ~ 35 μ m. (c) Volume rendering of a cubic field-of-view within stacked TXM slices. Elongated Al₃Ti is present along with clusters of TiC particles.

Small clusters of TiC particles were observed to surround the Al_3Ti in many cases, which becomes more apparent when looking at the reconstructed 3D volumes (Figure 1(c)) where TiC particles appear to be attached to the surface of the Al_3Ti (at the spatial resolution of TXM, 50 nm). The overall volume fraction of Al_3Ti was generally low, with < 0.5 vol pct per batch (as averaged from all SEM and TXM datasets for a given batch). In a similar sense, the C-rich regions (Figure 2(b)) exhibit a layer of TiC or cluster of particles surrounding them (on the order of tens of nm between C-rich regions and the surrounding TiC). Amounts of excess C were difficult to identify reliably *via* image recognition methods due to contrast similarities with pores and any contamination, but in general we observe < 0.02 vol pct per batch (as

averaged from all SEM and TXM datasets for a given batch). We also detected individual TiC particles as well as solid and ring-like clusters, as shown in Figures 2(b) and (c). The particles were largely spheroidal in shape, as confirmed by both SEM and the TXM observations, with some more ellipsoidal shapes also being present. The average TiC yield from SHS was estimated to be in the range of 1 to 2 vol pct, with particle sizes ranging from approximately 380 to 910 nm (as averaged from all SEM and TXM datasets for a given batch). It is also worth noting that although C/TiC and Al₃Ti/TiC features were observed, we did not see instances of C-rich regions in close proximity with Al₃Ti precipitates. Typically, excess C and Al₃Ti were separated by distances on the order of tens of micrometers.

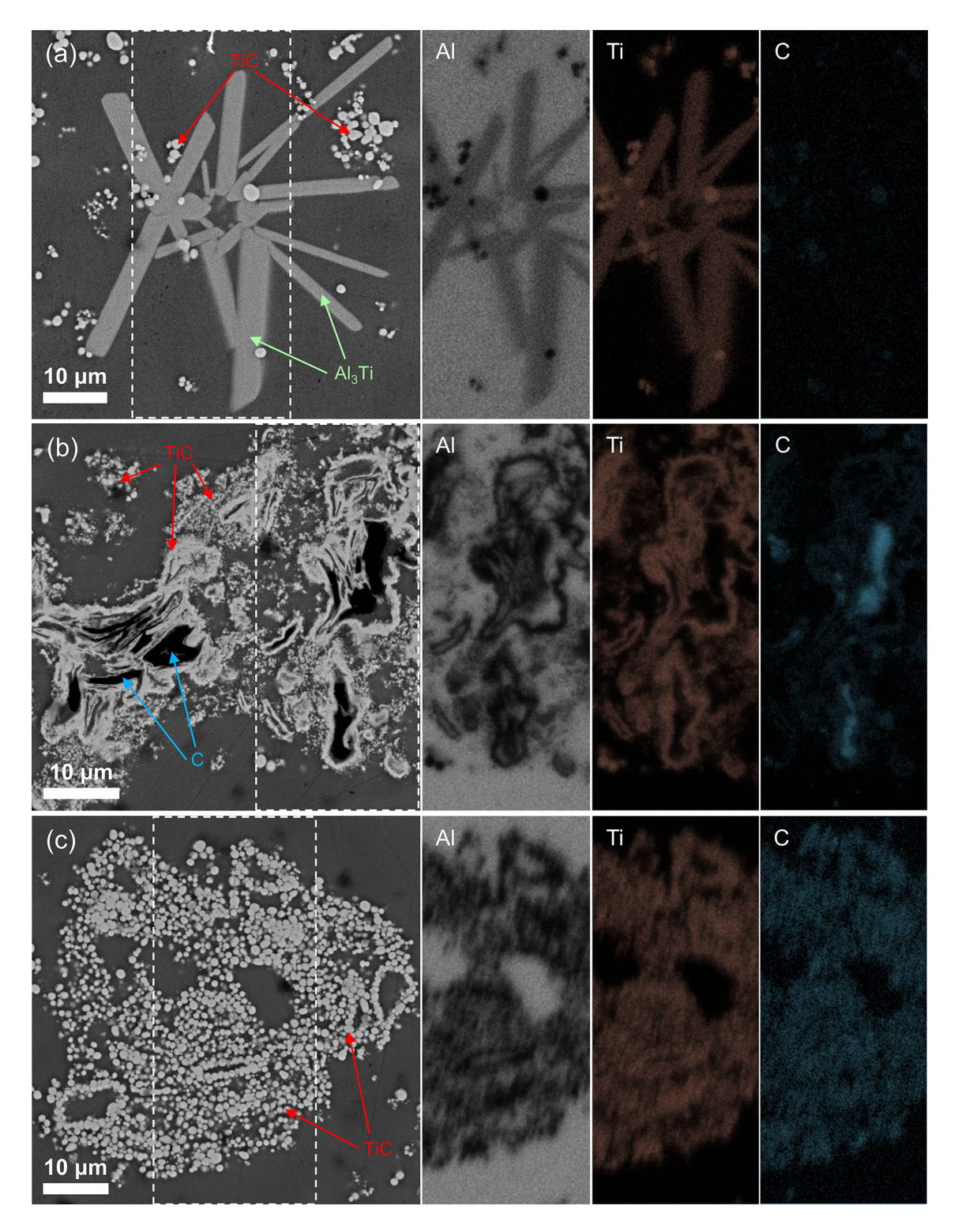


Fig. 2—SEM observations and corresponding EDS maps (EDS spectra taken from area enclosed by the dashed box): (a) Al₃Ti intermetallics with surrounding TiC particles; (b) C-rich regions with surrounding TiC particles; (c) clustered and individual TiC particles.

B. Thermodynamics of TiC Formation

In the CuO-assisted SHS process, the highly exothermic thermite reaction is thought to facilitate the high local temperatures typically needed for TiC formation, but estimates as to the peak reaction temperature vary. Theoretical calculations by Fischer and Grubelich^[36]

report an adiabatic peak reaction temperature of ~ 2800 K (2527 °C) accounting for phase change of the reaction products, while Lee *et al.*^[34] used a Gibbs formulation model^[37] to predict a peak temperature of ~ 4500 K (4227 °C) in liquid aluminum. Experimental measurements indicate that peak reaction temperatures are

dependent on bulk melt temperature, with a peak temperature of 1300 K (1027 °C) for a bulk temperature of 1023 K and 2000 K (750 °C and 1727 °C) for a bulk temperature of 1193 K (920 °C). Discrepancies in the experimental values are likely due to difficulties in measuring highly localized and transient thermal fields, as well as local variations in thermal conductivity in the pellet/melt system. Therefore, it is worth considering the thermodynamics of the SHS process over a relatively large temperature range to adequately account for bulk and peak temperatures.

TiC can form *via* SHS reaction according to indirect or direct reaction pathways.^[9] *Indirect* formation of TiC can occur by reaction between solutes and intermediate compounds, as given by

$$3[Ti] + Al_4C_3(s) = 3TiC(s) + 4Al(1),$$
 [1]

$$[C] + Al_3Ti(s) = TiC(s) + 3Al(1),$$
 [2]

or by solid-solid reactions between Ti- and C-based intermediate compounds,

$$C(s) + Al_3Ti(s) = TiC(s) + 3Al(l),$$
 [3]

$$3Al_3Ti(s) + Al_4C_3(s) = 3TiC(s) + 13Al(s).$$
 [4]

Alternatively, TiC can also be formed *directly via* solute-solute reaction or solute-precursor C reaction,

$$[Ti] + [C] = TiC(s),$$
 [5]

$$[Ti] + C(s) = TiC(s).$$
 [6]

Following Rapp and Zheng,^[38] we plot the Gibbs free energies of the various chemical reactions as well as solute generation from Ti and C sources for comparison in Figures 3(a) and (b). Several of the energy lines have been truncated based on the stable temperature ranges of the compounds involved in indirect reaction processes (e.g. the lines involving Al₃Ti(s) are truncated approximately at its melting temperature). All reactions appear thermodynamically favorable over the range of relevant temperatures, offering the possibility of multiple pathways in the formation of TiC (Figure 3(a)). However, the generation of [C] solutes necessary for Eqs. [2] and [5] requires temperatures in excess of ~ 1500 K (1227 °C).

C. Discussion of TiC Formation Pathways

The observed microstructural signatures and thermodynamics allow us to infer the dominant reaction pathways for TiC formation. The presence of Al₃Ti and the aforementioned TiC clustering around Al₃Ti (Figure 1(c)) are suggestive of reaction by Eqs. [2] and [3]. It is possible that the close proximity is due to both particles and intermetallics being pushed during solidification, but it may also be indicative of particle growth from the intermetallics themselves. Similar clustering behavior has been observed previously and attributed to

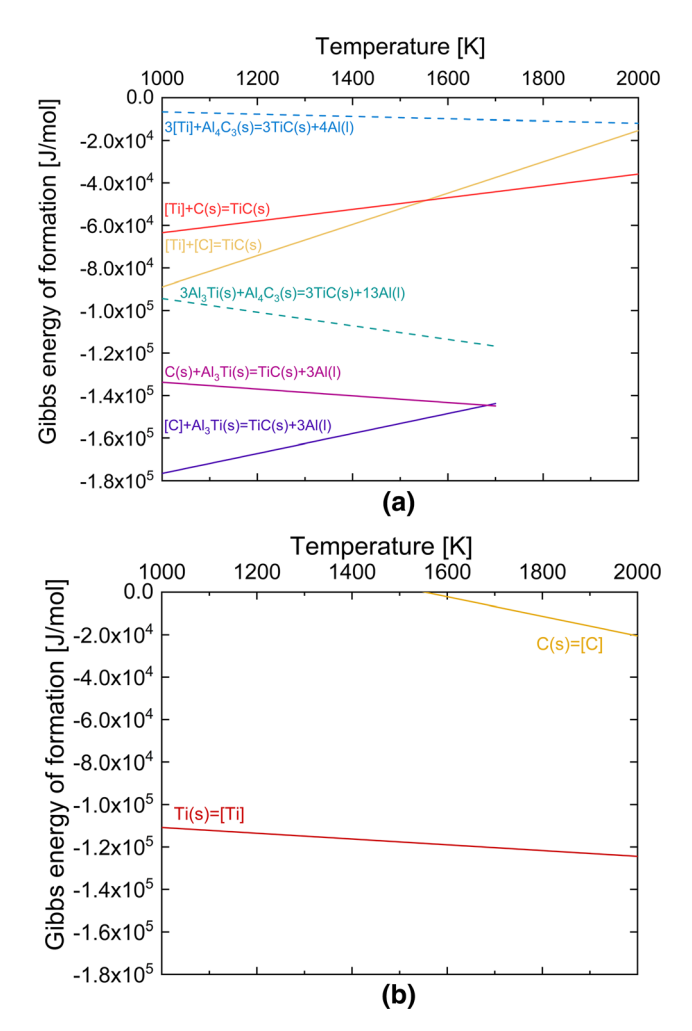


Fig. 3—Thermodynamic analysis based on equations from Rapp and Zheng^[38]: (a) Gibbs energies of formation for the various SHS reaction pathways over an operating temperature range covering bulk melt temperature and peak thermite reaction temperature. "Direct" reaction pathways are warm colored lines, "indirect" reaction pathways are cool colored lines. Dotted lines represent those reaction pathways that are ruled out as unlikely (see text for details). Some lines have been truncated based on maximum limits of phase stability. (b) Gibbs energies of formation for C and Ti solutes ([C] and [Ti]).

both Al₃Ti-based reaction pathways. ^[9,24,39,40] However, reaction *via* Eq. [2] may be more favorable than Eq. [3], as the solid-solid reaction has been observed to occur over relatively long time scales (on the order of hours for TiC formation from C and Al-Ti intermetallics). ^[41] Furthermore, solid-solid reaction processes are expected to be heavily dependent on the surface contact area between the two solid phases, ^[42] which may be impacted by factors such as localized turbulence in the melt during the self-propagating reaction. The lack of observed Al₃Ti and C in contact with each other, or any indication of partial reaction, would also agree with Eq. [3] either not occurring here or else occurring in a limited capacity.

The observation of TiC particles forming around C-rich regions (Figure 2(b)) may be indicative of partial reaction or nucleation sites, thus suggesting that Eq. [6]

is also plausible. Numerous observations have been made of TiC surrounding excess C after SHS reaction, and they are often attributed to dissolution of Al_3Ti and subsequent [Ti]-C(s) reaction. [9,22,23]

Reactions involving Al₄C₃ (Eqs. [1] and [4])) may be unlikely here, given that it is absent in any of the batches in either a partially reacted or standalone state. Banerji and Reif^[43] proposed that Al₄C₃ may be more stable than TiC below temperatures of 1500 K (1227 °C), in which case we would expect residual Al₄C₃, but this was disputed^[38,44] and found to be valid only for very low levels of dissolved Ti. It is likely that the concentration of dissolved Ti is higher than the concentration of dissolved C in the melt during processing, considering the more favorable dissolution of Ti (Figure 3(b)) over the operative temperature range. Additionally, the highest thermite reaction temperatures (> 1500 K) are required to initiate any C dissolution and, despite discrepancies in the peak reaction temperature, the heat around a CuO reaction site dissipates rapidly (~ 1 ms).[34,45] Furthermore, on the Al-rich side of the phase diagram and at concentrations of high Ti relative to C, the Al₄C₃ phase does not co-exist with TiC, Al₃Ti, and liquid Al. Therefore, reaction pathways involving Al₄C₃ are improbable or limited as compared with other mechanisms.

The direct reaction of [Ti] and [C] in Eq. [5] is difficult to confirm or rule out directly, as no residual evidence of the reaction would be expected or observed. However, Eq. [5] becomes thermodynamically favorable at high temperatures where the dissolution of C is facilitated. It is possible that the particle clusters observed (Figure 2(c)), without C-rich regions present, are suggestive of the direct [Ti]-[C] mechanism occurring with a higher frequency in localized regions around thermite reaction sites. Additionally, individual TiC particles observed separate from other solid phases or clusters may also be the result of reaction via Eq. [5], occurring when isolated solutes interact after diffusing away from reaction sites.

Figure 4 is a schematic that surveys the dominant formation mechanisms of TiC. In the process, the compacted pellet consisting of Al-Ti-C-CuO powders is plunged directly into an Al melt between 1043 K and 1133 K (770 °C and 860 °C). Subsequently, Al powders will begin to melt and react with the solid Ti particles and begin to form Al₃Ti, which is expected at these temperatures even in the absence of thermite. [47-49] The liquid Al will then reduce the CuO thermite, quickly increasing the local temperature upwards of 1500 K (1227 °C). Al₃Ti (s) and C (s) will subsequently break down and form dissolved [Ti] and [C] in the melt near the thermite reaction sites. At this point [C], [Ti], Al₃Ti(s), and C(s) co-exist in the melt and three reaction pathways can take place in series or in parallel according to Eqs. [2], [5], and [6]). Consequently, we expect to see a final microstructure consisting of TiC particles (both individual and clustered), Al₃Ti intermetallics, and excess C-rich regions.

IV. CANONICAL CORRELATION ANALYSIS

A. Motivation

To assist in reconciling the wide variety of processing conditions (Table I), microstructural observations (Figures 1 and 2), and potential formation pathways (Figure 4), we conducted a canonical correlation analysis (CCA). Broadly, CCA is a multivariate statistical model used to study linear associations between two sets of variables *via* analysis of the cross-covariance matrices. [50] As compared with multiple regression, CCA has the advantage of being able to handle multiple dependent variables simultaneously. [50,51] The methodology of CCA has been discussed in detail elsewhere, [50–56] but will be briefly described here for the purpose of defining key terms.

CCA assumes a set of x_i input and y_i output variables,

$$\vec{X} = \{x_1, x_2, x_3, \dots x_i\},$$
 [7]

$$\bar{Y} = \{y_1, y_2, y_3, \dots y_j\},$$
 [8]

where subscripts i and j correspond to the number of input and output variables respectively. Ultimately, CCA seeks to identify linear combinations (up to a maximum of i = j) of artificial variables, otherwise known as *canonical variates*, that exhibit maximum correlations (*canonical correlations*). Canonical variates are denoted as

$$V = \sum_{i} \alpha_{i} x_{i},$$
 [9]

$$W = \sum_{j} \beta_{j} y_{j}, \qquad [10]$$

where V and W are the canonical variates and α and β are weighted coefficients, known as canonical weights. Effectively, the *weights* used in the canonical variates represent the relative contributions of each independent variable to the dependent variables, at a maximized canonical correlation. Additional quantities of interest for our analysis include the canonical loadings (or cross-loadings), and the redundancy indices. [50] The canonical loadings and cross-loadings are a measure of the correlation between the original variables used in the analysis and the canonical variates. [57] Redundancy indices provide a means of interpreting the shared variance of the canonical variates (i.e., r^2). Thus, to assess the overall "goodness" of the analysis and interpret the results, all of these factors must be considered holistically. Standard statistical significance testing can also be used to aid in interpretation and evaluation of robustness of the CCA results (such as the Wilks–Lambda significance test). [50–52]

B. Parameters and Definitions

Below we define our input and output variables. For input metrics \vec{X} , we use the processing parameters (from

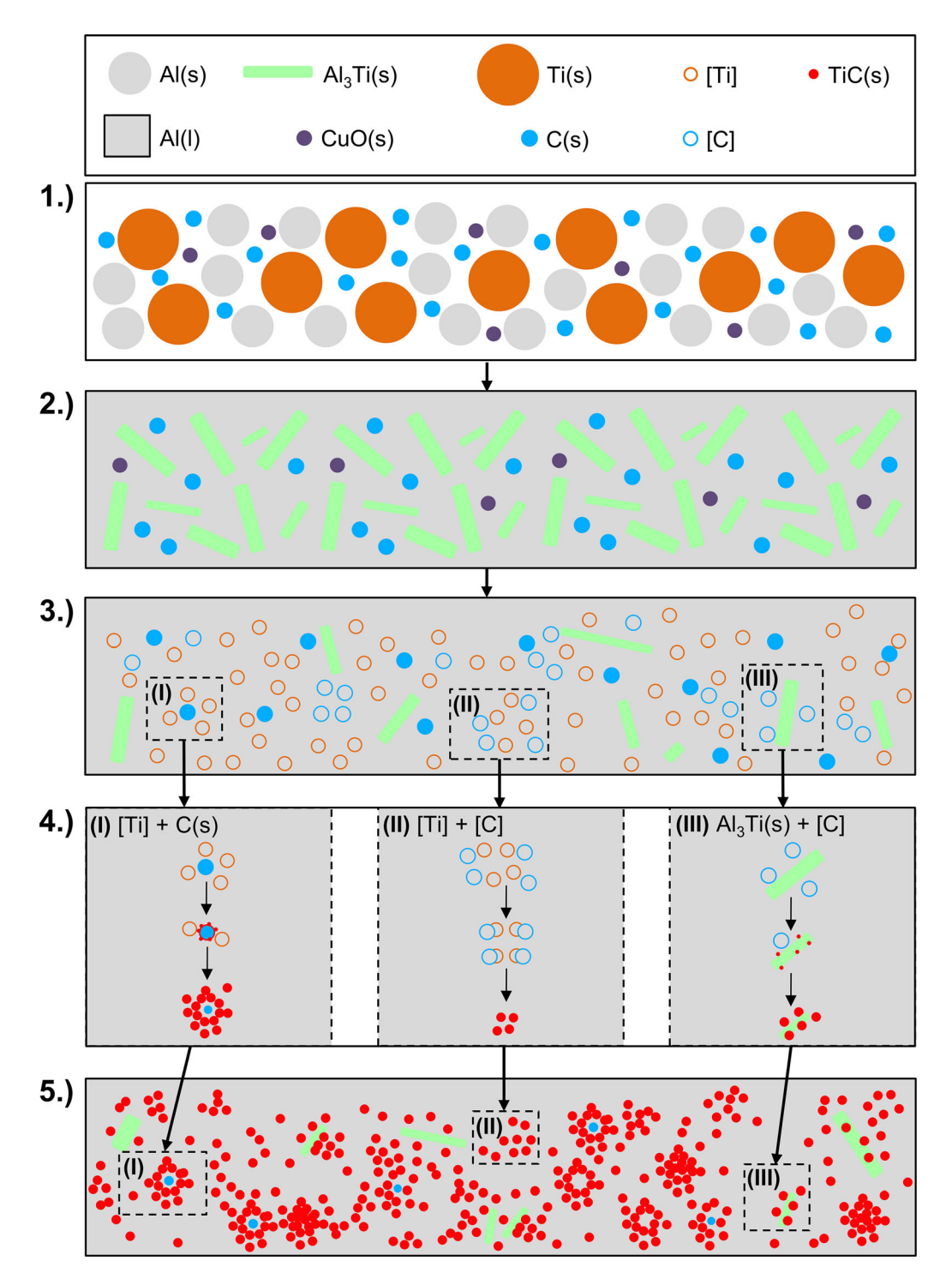


Fig. 4—Schematic depicting formation mechanisms of TiC *via* thermite-assisted SHS reactions. Upon insertion of a pellet to the melt (1), Al melts and forms intermediate Al₃Ti precipitates (2). The CuO thermite subsequently reacts with liquid Al and a sharp temperature increase (> 1500 K) causes dissolution of solid C particles and Al₃Ti precipitates (3). TiC formation then occurs *via* one of three parallel reaction pathways (4), yielding distinct microstructural signatures (5). All suggested pathways are consistent with experimental observations (*cf.* Figs. 1 and 2).

Table I): bulk melt temperature (T_{proc}), C and CuO pellet composition (n_{C} , n_{CuO}), Ti precursor size (d_{Ti}), pellet packing method, powder mixing method, and powder/melt mass ratio ($r_{\text{p/m}}$). For the output metrics

 \bar{Y}_1 , we choose volume percentage of TiC (v_{TiC}), average diameter of TiC particles (d_{TiC}), and volume percentage

of Al₃Ti intermetallic phases ($v_{\text{Al}_3\text{Ti}}$). The choice of output metrics here is based on our microstructural observations (Figure 2) with the goal of informing process parameters in tuning TiC characteristics. Although volume percentage of excess C (Figure 2(b)) was also an observed microstructural feature, it was not included here due to the very low volumes relative to

TiC and Al₃Ti (< 0.02 vol pct based on an average of all SEM and TXM datasets for a given batch). A second grouping of relevant output metrics \bar{Y}_2 was also identified, consisting of dispersion (*D*), agglomeration (*A*), and Al₃Ti volume percentage (v_{Al_3Ti}).* The ratio-

*We create two separate canonical variates (denoted as \bar{Y}_1 and \bar{Y}_2) in order to avoid the problem of multicollinearity^[50] between the dependent variables.

nale behind this particular set of variables was to provide some indication as to whether different processing conditions lead to different reaction pathways (*e.g.*, TiC formed *via* [Ti]-[C] may be more dispersed, whereas agglomerated TiC or high Al₃Ti vol pct may indicate more solid-solute mediated reaction mechanisms). Additionally, dispersion and agglomeration are microstructural features of interest due to their strong influence on the overall mechanical performance of MMNCs.^[58–60]

Dispersion, D, and agglomeration, A, were calculated for each 2D/3D dataset using the approach developed by Tyson *et al.*^[61] First probability density functions (PDFs, denoted as f in the equations that follow) were created from the distributions of particle diameters and interparticle spacings^[62] in the image. Then, D and A were found as,

$$D = \int_{0.8\mu}^{1.2\mu} f(r_{\text{TiC-TiC}}) dr,$$
 [11]

$$A = 1 - \int_{0.7\mu}^{1.3\mu} f(d_{\text{TiC}}) dd,$$
 [12]

where $r_{\text{TiC-TiC}}$ is the nearest-neighbor interparticle spacing, d_{TiC} is the particle diameter, and μ is the mean value of each corresponding PDF. In the limit the particles are perfectly disperse and not clustered, D=1

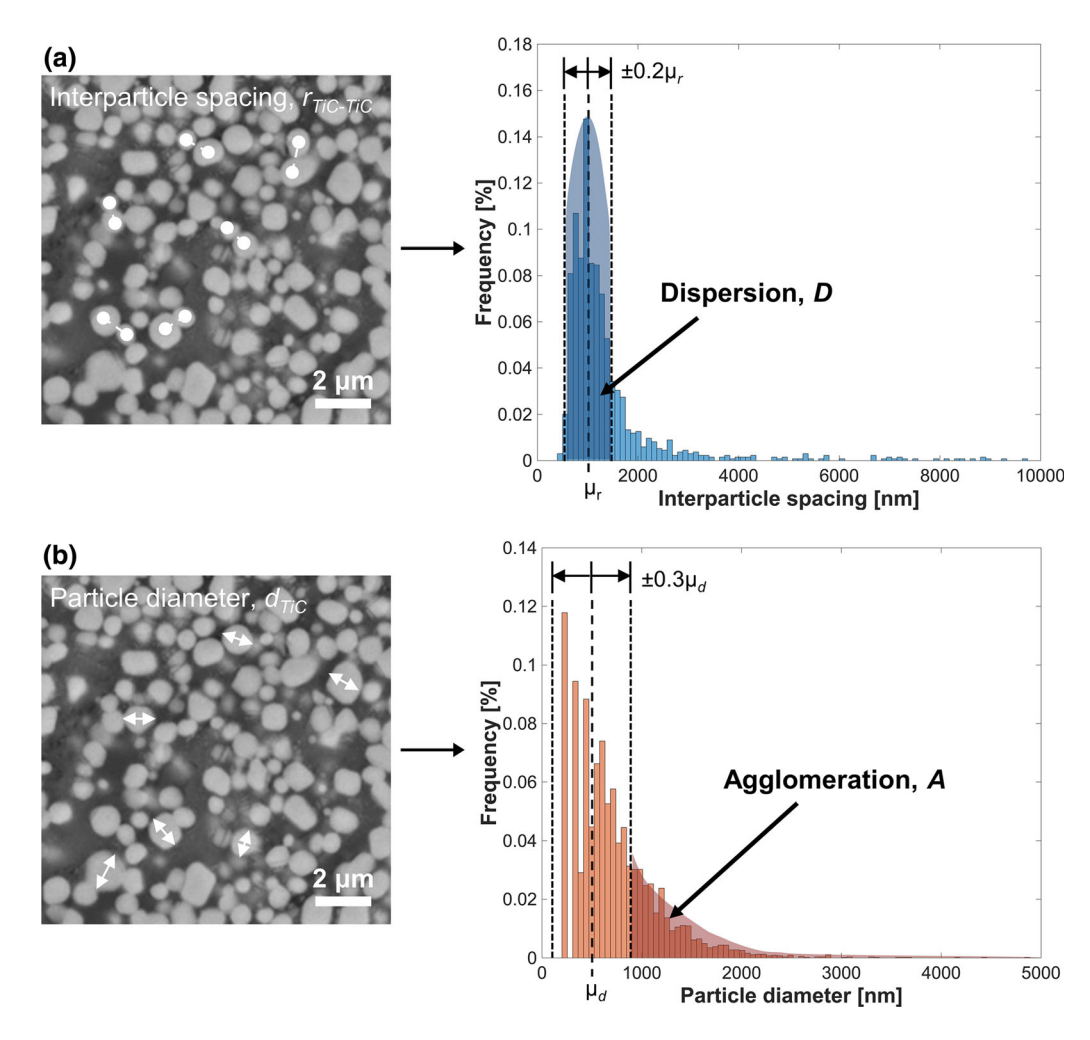


Fig. 5—(a) Example calculation of particle dispersion, D, based on a corresponding probability distribution function of interparticle spacings. (b) Example calculation of particle agglomeration, A, based on a corresponding probability distribution function of particle diameters. SEM images at left are high-magnification representations to more clearly show the definitions of interparticle spacing and diameter (lower magnification images are used to construct the PDFs so that a sufficient number of particles can be captured). In general, > 1200 particles are considered in constructing the probability distributions. See text for computational details.

and A=0 (and *vice versa* in the opposite limit). A graphical representation of how dispersion and agglomeration are calculated is shown in Figure 5(a) and (b), for a representative high-magnification SEM image.

CCA was carried out using the CCA package developed by González et al. [63] for the R statistical computing environment. We used a sample size of 200 observations (i.e., 20 times the number of variables) corresponding to both SEM and TXM datasets (where one observation represents complete particle and intermetallic statistics for a single SEM image or TXM volume, taken from different locations of ingots from each batch). The CCA input data (e.g. particle diameter, volume percentage, etc.) was compiled from calculations using the image processing methods described in Section II—C.

C. Results and Discussion

CCA evaluation of the first group of variables Y_1 using v_{TiC} , d_{TiC} , and v_{Al_3Ti} as the dependent variables yield linear combinations with correlation coefficients of 0.74, 0.18, and 0.11. The relative differences between the coefficients, as well as a redundancy index analysis, suggest that the first pair of canonical variates is sufficient to describe the data. A table of the relevant results for the first canonical variate pair is shown in Table II and the variates are plotted together in Figure 6 (SEM data in blue and TXM data in red). A least squares fit to the data and the relatively high correlation coefficient suggest that the behavior of the dependent variate, W, is reasonably well described by the independent variate, V. A Wilks-Lambda test yields p < 0.001, indicating the results are statistically significant. A graphical representation of the absolute value of the loadings and weights for each variable is shown in Figure 7, where the relative diameters of the circles correspond to the variance (squared loadings). Variables with high weights and significant loadings (≥ 0.40 for sample sizes of at least 200^[50,57]) are considered to dominate the behavior of the variate. Thus, the dominant variables for further consideration can be reduced to the independent variables $n_{\rm C}$, $r_{\rm p/m}$, and the dependent variable $v_{\rm TiC}$.

CCA evaluation of the second group of variables Y_2 with D, A, and $v_{\rm Al_3Ti}$ as dependent variables yield linear combinations with correlation coefficients of 0.82, 0.42, and 0.15 for the first, second, and third canonical variate pairs respectively. Similar to the first group of metrics, we assume the first canonical variate pair is sufficient for interpretation of the CCA based on the relative magnitudes of r^2 and a redundancy index analysis. A Wilks–Lambda test suggests the first canonical correlation is statistically significant, yielding p < 0.001. A summary of the relevant results for the first variate pair is shown in Table III and a least squares fit and the correlation coefficient suggest that W is well described by V (Figure 8). A graphical representation of the absolute value of the loadings and weights for each

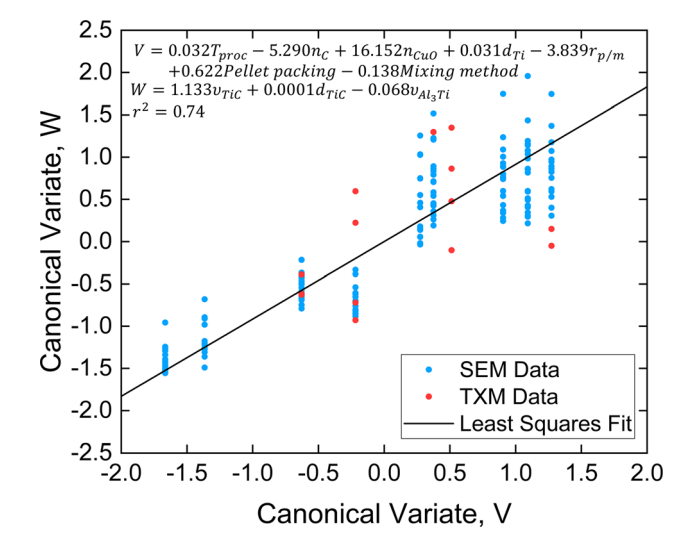


Fig. 6—Correlation of the canonical variates using the output metrics $v_{\rm TiC}$, $d_{\rm TiC}$, and $v_{\rm Al_3Ti}$ (metric set Y_1) in canonical variate W. Data points are colored according to the experimental probe used to capture the microstructure (either SEM or TXM, see Fig. 1). The associated canonical weights of each variate and the canonical correlation coefficient are shown at the top left.

Table II. Summary of the CCA Analysis Using TiC Particle Volume Percentage (v_{TiC}), TiC particle diameter (d_{TiC}), and Al₃Ti Intermetallic Volume Percentage ($v_{\text{Al}_3\text{Ti}}$) (metric set \bar{Y}_1) as the Dependent Variables for the Output Metrics

Variable	Weight	Loading	Cross-Loading	Redundancy Index
T_{proc}	0.032	0.888	0.761	0.401
$n_{\rm C}$	-5.290	-0.651	-0.558	
n_{CuO}	16.152	-0.386	-0.331	
d_{Ti}	0.031	0.869	0.745	
$r_{\rm p/m}$	-3.839	0.811	0.696	
Pellet Packing	0.622	0.643	0.551	
Mixing Method	-0.138	-0.794	-0.680	
$V_{ m TiC}$	1.133	0.999	0.857	0.275
d_{TiC}	-0.0001	0.336	0.288	
$V_{\mathrm{Al_3Ti}}$	-0.068	0.096	0.083	

The input variable metrics are bulk melt temperature (T_{proc}), C and CuO pellet composition (n_{C} , n_{CuO}), Ti precursor size (d_{Ti}), pellet packing method, powder mixing method, and powder/melt mass ratio ($r_{\text{p/m}}$) and the redundancy indices apply to all the inputs (for 0.401) and outputs (0.275).

variable is shown in Figure 9. Based on the significant weights and loadings, the independent variables n_{CuO} , n_{C} , and $r_{\text{p/m}}$ dominate the behavior of V, while the behavior of W is not observed to be dominated by a specific variable (although D exhibits the highest weight and loading).

The results of both CCAs suggest that the amount of precursor powder ($n_{\rm C}$ and $r_{\rm p/m}$) and the amount of thermite, $n_{\rm CuO}$, have the largest impact on the final microstructure (e.g., TiC characteristics and distribution). Several of the variables in the independent variate \bar{X} ($T_{\rm proc}$, $d_{\rm Ti}$, pellet packing method, and powder mixing method) exhibit a high loading, but low weight (relative to the dominant variables).. This suggests that these

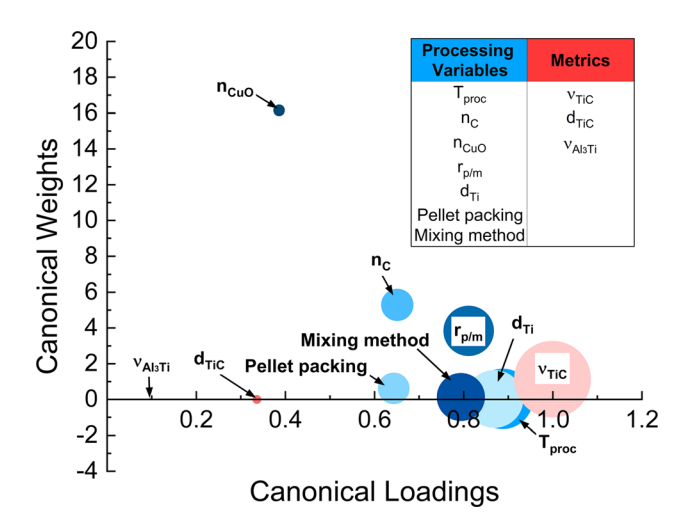


Fig. 7—Graphical representation of the CCA-determined weights and loadings (of the first canonical variate pair) using $v_{\rm TiC}$, $d_{\rm TiC}$, and $v_{\rm Al_3Ti}$ (metric set \bar{Y}_1) as the output metrics. The diameter of each circle corresponds to the fraction of the variance associated with each variable (squared loadings). Relatively higher weights and loadings for $n_{\rm C}$ and $r_{\rm p/m}$ indicate that they explain a larger fraction of the canonical variate of processing variables, V. The relatively higher loading for $v_{\rm TiC}$ indicates that it explains a large fraction of the canonical variate of output metrics, W. A more detailed list of the CCA outputs is found in Table II.

variables are accurately captured by the independent variates and that the dependent variates \vec{Y}_1 and \vec{Y}_2 are weakly sensitive to variations in these inputs. The relatively low weights calculated for the dependent variates in both CCAs may stem from non-linear relationships between the outputs and the inputs that may be more accurately captured by supplementary methods such as a Monte Carlo analysis. [56] Nevertheless, the high correlation coefficients between the variates in both CCAs suggest a measure of sensitivity in the output variables to the dominant input variables.

The results of the CCA are in agreement with our microstructural observations and the thermodynamics of TiC formation (Section III), suggesting that the amount of C and CuO have the largest impact (relative to the other processing variables) on the final microstructure. In our schematic (Figure 4) of

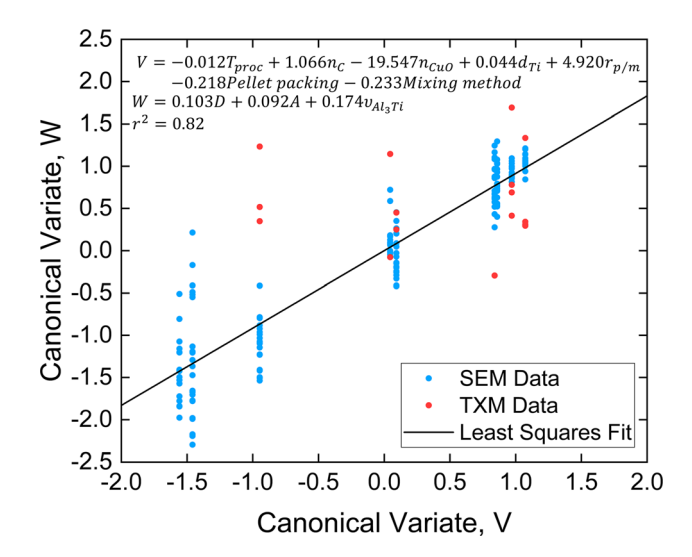


Fig. 8—Correlation plot of the canonical variates using the output metrics D, A, and v_{Al_1Ti} (metric set \bar{Y}_2) in canonical variate W. Data points are colored according to the experimental probe used to capture the microstructure (either SEM or TXM, see Fig. 1). The associated canonical weights of each variate and the correlation coefficient are shown at top left.

Table III. Summary of the CCA Analysis Using Particle Dispersion (D), Particle Agglomeration (A), and Volume Percentage of Al₃Ti Intermetallics (v_{Al_3Ti}) (metric set \bar{Y}_2) as the Dependent Variables for the Output Metrics

Variable	Weight	Loading	Cross-Loading	Redundancy Index
$T_{ m proc}$	-0.012	0.902	0.816	0.445
$n_{\rm C}$	1.066	-0.488	-0.441	
n_{CuO}	-19.547	-0.855	-0.773	
d_{Ti}	0.044	0.931	0.842	
$r_{\rm p/m}$	4.920	0.787	0.711	
Pellet Packing	-0.218	0.563	0.509	
Mixing Method	-0.233	-0.475	-0.430	
D	0.103	0.639	0.577	0.180
A	0.092	0.461	0.416	
v_{Al_3Ti}	0.174	0.198	0.179	

The input variable metrics are bulk melt temperature (T_{proc}), C and CuO pellet composition (n_{C} , n_{CuO}), Ti precursor size (d_{Ti}), pellet packing method, powder mixing method, and powder/melt mass ratio ($r_{\text{p/m}}$) and the redundancy indices apply to all the inputs (for 0.445) and outputs (0.180).

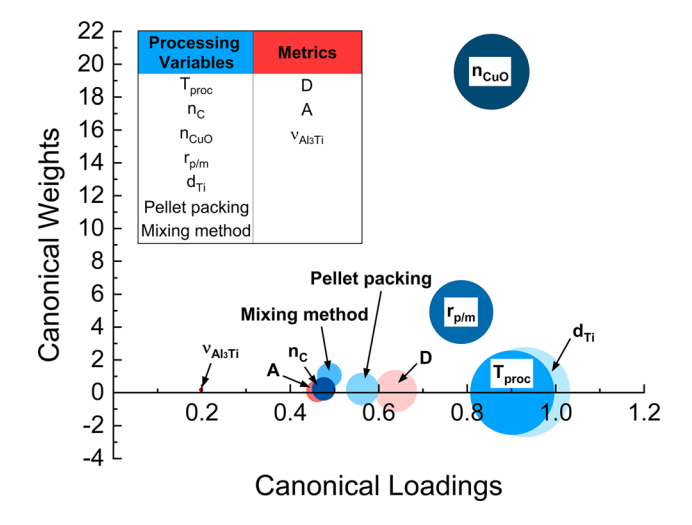


Fig. 9—Graphical representation of the CCA determined weights and loadings (of the second canonical variate pair) using D, A, and $v_{\rm Al_3Ti}$ (metric set $\bar{\rm Y}_2$) as the output metrics. The diameter of each circle corresponds to the fraction of the variance associated with each variable (squared loadings). Relatively higher weights and loadings for $n_{\rm CuO}$, $n_{\rm C}$ and $r_{\rm p/m}$ indicate that they explain a large fraction of the canonical variate of processing variables, V, in agreement with results obtained from the other canonical variate pair (Fig. 7). The relatively similar weights and sufficiently high loadings of dispersion and agglomeration indicate that they explain roughly equal fractions of the canonical variate of output metrics, W. A more detailed list of the CCA outputs is found in Table III.

formation mechanisms, we proposed three dominant reaction pathways (all requiring C) consisting of TiC formation via direct mechanisms (i.e., [Ti] and [C] or solid C interactions, Figures 2(b) through (c)) and an indirect mechanism (i.e., [C] with Al₃Ti, Figures 1(a) and 2(a)). However, based on the thermodynamics (Figures 3(a) and (b)), it is expected that only the reaction pathway involving [Ti] and solid C will be favorable below temperatures of ~ 1500 K (1227 °C). Thus, the amount of CuO will play a dominant role in TiC formation as the high temperatures required for [C] dissolution and initiation of the other two formation pathways (i.e., [Ti]-[C] and [C]-Al₃Ti) are dependent on the availability of thermite reaction sites. Given that the three pathways exhibit distinct microstructural signatures, tuning the characteristics of the CuO (e.g., amount, particle size, distribution within the pellet) may provide a more effective measure of microstructural control.

D. Considerations of Morphological Evolution

The combined CCA and microstructural data shown above provide a holistic view of the key processing variables and hypothetical reaction pathways for the formation of TiC. We have not yet considered on a more local scale the morphological evolution of individual phases *via* each pathway, which can also have a significant impact on physical properties. In particular, the shape of the reinforcing and secondary phases (*e.g.*, the TiC particles and Al₃Ti intermetallics here) have been found to strongly affect the mechanical performance of the material. [64–66]

The TiC particles observed here (See Figures 1(c) and 2) are typically spheroidal or nearly spheroidal (e.g., ellipsoidal) in shape. Jin et al., [67,68] Dong et al., [69] and Zhang et al. [70] have demonstrated that the shape of TiC is heavily influenced by the stoichiometric ratio of C/Ti, where a perfect sphere corresponds to C/Ti ~1.0 and sub-stoichiometric ratios of C/Ti can lead to cubic (C/Ti > 1.0), ellipsoidal (C/Ti < 1.0), or octahedral (C/Ti \ll 1.0) morphologies. Particles corresponding to C/Ti stoichiometry close to 1.0 would be in good agreement with the morphologies observed here (See Figure 3(b)). The presence of some ellipsoidal particles corresponding to C/Ti < 1.0 (i.e., TiC_{x<1}) may be due to instances of particle formation that are C limited (e.g., reaction via Eq. [5]). However, it is also possible that some of these ellipsoidal particles may change to spherical over time. Previous studies of TiC formation in Al via SHS reaction have observed particle evolution from octahedral to ellipsoidal and spherical, owing to a thermodynamic roughening transition from (111) stable particle surfaces to (100) stable surfaces. [67,69]

Similarly, the Al₃Ti morphology has been shown to be highly sensitive to processing conditions, with primarily either the blocky/platelet-like (both elongated and equiaxed) or needle-like flakey morphologies forming based on melt processing temperature, cooling rate, and Ti concentration. The Al₃Ti intermetallics in this study exhibit an elongated shape with some degree of faceting at the ends (See Figures 1(c) and 2(a)). Faceting is likely a characteristic of platelet-type Al₃Ti, which has been observed to form at relatively low processing temperatures (as low as ~ 730 °C). [47,71,76] Observed platelets may be consistent with formation by reaction between the surrounding liquid Al, melting Al powders, and solid Ti powders when the pellets are introduced into the melt (between 770 °C and 860 °C in this study). Alternatively, Zhao *et al.*^[75] and Arnberg *et al.*^[71] have attributed the blocky faceted formation to a local supersaturation of Ti. This explanation may also be feasible, given that high local Ti concentrations arise following CuO reaction and melting of nearby Ti powders. In general, elongated faceted intermetallics are suggestive of anisotropic growth, which has been hypothesized to occur preferentially in the (110) direction due to nucleation on lowest density atomic planes. [72,77,78]

For both TiC particles and Al₃Ti intermetallics, different morphological evolution pathways may still lead to the same morphologies in the final microstructure (*e.g.*, direct formation of spherical TiC particles *vs* roughening transitioning from octahedral to spherical particles). However, each pathway may be sensitive to the processing conditions and occur at different or competing rates; such intermediate steps cannot be accessed using the present analysis. To supplement our investigation, a complimentary approach such as phase field modeling^[79] or reaction-diffusion modeling^[80] of SHS reaction would be illuminating. *In situ* studies of microstructure formation (through, *e.g.*, TXM^[81]) would also help validate and refine these models. The time-resolved experiments and models would provide a

more complete picture of the morphological evolution underlying complex reactive processes.

V. CONCLUSIONS

We have analyzed in situ Al/TiC MMNCs produced via thermite-assisted SHS. A variety of processing conditions were studied and the microstructure characterized by both SEM and TXM (2D and 3D) to better understand TiC particle formation. By corroborating the microstructural data with thermodynamic analyses, we have proposed a formation mechanism for SHS TiC consisting of three reaction pathways that lead to distinct microstructural signatures. We have also conducted CCA on the data collected in our study and demonstrated its potential as a means of guiding processing parameter choice for production of SHS MMNCs. The results of this study on the formation mechanisms and processing input/output relationships will inform future SHS experiments and the rational design of in situ SHS MMNCs.

ACKNOWLEDGMENTS

This research used resources of the Advanced Photon Source, a U.S. Department of Energy (DOE) Office of Science User Facility operated for the DOE Office of Science by Argonne National Laboratory under Contract No. DE-AC02-06CH11357. The authors gratefully acknowledge financial support from the Melt R2-2 project funded by LIFT (Lightweight Innovations For Tomorrow), a Manufacturing Institute under the contract from the Office of Naval Research (Contract # N00014-14-2-002), as well as financial support from the National Science Foundation (Award # 1762657). The authors also acknowledge financial support from the University of Michigan College of Engineering and technical support from the Michigan Center for Materials Characterization. We also thank David Weiss at Eck Industries and Stephen Udvardy at the North American Die Casting Association for helpful discussions.

ELECTRONIC SUPPLEMENTARY MATERIAL

The online version of this article (https://doi.org/10. 1007/s11661-020-05786-1) contains supplementary material, which is available to authorized users.

REFERENCES

1. R. Geng, F. Qiu, and Q.C. Jiang: *Adv. Eng. Mater.*, 2018, vol. 20, pp. 1–13.

- 2. E.D. Moor, A. Luo, D.K. Matlock, J.G. Speer, and A. Taub: *Annu. Rev. Mater. Res.*, 2000, vol. 49, pp. 1–33.
- A. Mortensen and J. Llorca: Annu. Rev. Mater. Res, 2010, vol. 40, pp. 243–70.
- 4. A.V. Muley, S. Aravindan, and I.P. Singh: *Manuf. Rev.*, 2015, vol. 2, p. 15.
- S.L. Pramod, S.R. Bakshi, and B.S. Murty: J. Mater. Eng. Perform., 2015, vol. 24, pp. 2185–2207.
- 6. D.K. Das, P.C. Mishra, S. Singh, and S. Pattanaik: *Int. J. Mech. Mater. Eng.*, 2014, vol. 9, pp. 1–15.
- J. Hashim, L. Looney, and M.S.J. Hashmi: *J. Mater. Process. Technol.*, 2001, vol. 119, pp. 324–28.
- 8. B.S.S. Daniel, V.S.R. Murthy, and G.S. Murty: *J. Mater. Process. Technol.*, 1997, vol. 68, pp. 132–55.
- 9. Y.H. Cho, J.M. Lee, and S.H. Kim: *Metall. Mater. Trans. A*, 2014, vol. 45, pp. 5667–78.
- I. Anza and M.M. Makhlouf: *Metall. Mater. Trans. B*, 2018, vol. 49, pp. 466–80.
- C. Borgonovo and M.M. Makhlouf: Metall. Mater. Trans. A, 2016, vol. 47A, pp. 5125–35.
- 12. C.H. Henager, J.L. Brimhall, L.N. Brush: *Mater. Sci. Eng.*, *A*, 1995, vol. 195, pp. 65-74.
- R. Radhakrishnan, S.B. Bhaduri, and C.H. Henager: Adv. PM Part., 1995, vol. 3, pp. 1–9.
- 14. M. Backhaus-Riccoult and H. Schmalzried: *Ber. Bunsenges. Phys. Chem.*, 1985, vol. 89, pp. 1323–30.
- M. Martin and H. Schmalzried: Ber. Bunsenges. Phys. Chem., 1985, vol. 89, pp. 124–30.
- S.-B. Li, J.-X. Xie, L.-Y. Zhang, and L.-F. Cheng: *Mater. Sci. Eng. A*, 2004, vol. 381, pp. 51–56.
- A. Zhou, C.-A. Wang, Z. Ge, and L. Wu: J. Mater. Sci. Lett., 2001, vol. 20, pp. 1971–73.
- Y. Bai, X. He, Y. Li, C. Zhu, and S. Zhang: *J. Mater. Res.*, 2009, vol. 24, pp. 2528–35.
- R.F. Shyu and C.T. Ho: J. Mater. Process. Technol., 2006, vol. 171, pp. 411–16.
- C. Wang, H. Gao, Y. Dai, X. Ruan, J. Shen, J. Wang, and B. Sun: J. Alloys Compd., 2010, vol. 490, pp. 2009–11.
- Y.H. Cho, J.M. Lee, and S.H. Kim: Metall. Mater. Trans. A, 2015, vol. 46, pp. 1374–84.
- X.C. Tong and H.S. Fang: Metall. Mater. Trans. A, 1998, vol. 29A, pp. 875–91.
- E. Zhang, S. Zeng, B. Yang, Q. Li, and M. Ma: *Metall. Mater. Trans. A*, 1999, vol. 30A, pp. 1147–51.
- I. Gotman, M.J. Koczak, and E. Shtessel: *Mater. Sci. Eng. A*, 1994, vol. 187, pp. 189–99.
- V. De Andrade, A. Deriy, M.J. Wojcik, D. Gürsoy, D. Shu, K. Fezzaa, F. De Carlo: Nanoscale 3D imaging at the Advanced Photon Source (SPIE, 2016). Accessed 20 August 2019.
- C.S. Kaira, V. De Andrade, S.S. Singh, C. Kantzos, A. Kirubanandham, F. De Carlo, and N. Chawla: *Adv. Mater.*, 2017, vol. 29, pp. 1–8.
- J.H. Friedman, J.L. Bentley, and R.A. Finkel: *ACM Trans. Math. Softw.*, 1976, vol. 1549, pp. 1–38.
- 28. R. Keinan, H. Bale, N. Gueninchault, E.M. Lauridsen, and A.J. Shahani: *Acta Mater.*, 2018, vol. 148, pp. 225–34.
- 29. A.J. Shahani, X. Xiao, K. Skinner, M. Peters, and P.W. Voorhees: *Mater. Sci. Eng. A*, 2016, vol. 673, pp. 307–20.
- 30. D. Gürsoy, F. De Carlo, X. Xiao, and C. Jacobsen: *J. Synchrotron Radiat.*, 2014, vol. 21, pp. 1188–93.
- B.A. Dowd, G.H. Campbell, R.B. Marr, V.V. Nagarkar, S.V. Tipnis, L. Axe, D.P. Siddons: in *Dev. X-Ray Tomogr. II Conf. Proc.*, 1999, pp. 224–36.
- 32. D.M. Pelt and V. De Andrade: Adv. Struct. Chem. Imaging, 2017, vol. 2, pp. 1–14.
- 33. Y.-H. Cho, J.-M. Lee, H.-J. Kim, J.-J. Kim, and S.-H. Kim: *Met. Mater. Int.*, 2013, vol. 19, pp. 1109–16.
- 34. K. Lee, D.S. Stewart, M. Clemenson, N. Glumac, C. Murzyn: *AIP Conf. Proc.*, 2017, pp. 1–4.
- 35. P.C. Maity, P.N. Chakraborty, and S.C. Panigrahi: *Matt. Lett.*, 1997, vol. 30, pp. 147–51.
- S.H. Fischer, M.C. Grubelich: 32nd AIAA/ASME/SAE/ASEE Joint Propul. Conf. Proc., 1996, pp. 1–13.
- 37. D.S. Stewart: AIP, 2017, pp. 1-4.

- 38. R.A. Rapp and X. Zheng: *Metall. Trans. A*, 1991, vol. 22A, pp. 3071–75.
- N. Samer, J. Andrieux, B. Gardiola, N. Karnatak, O. Martin, H. Kurita, L. Chaffron, S. Gourdet, S. Lay, and O. Dezellus: Composites Part A, 2015, vol. 72, pp. 50–57.
- 40. H.Y. Wang, Q.C. Jiang, X.L. Li, and J.G. Wang: Scripta Mater., 2003, vol. 48, pp. 1349–54.
- 41. Q.C. Jiang, H.Y. Wang, Y.G. Zhao, and X.L. Li: *Mater. Res. Bull.*, 2005, vol. 40, pp. 521–27.
- 42. V.V. Dalvi and A.K. Suresh: *AIChE J.*, 2011, vol. 57, pp. 1329–38.
- 43. A. Banerji and W. Reif: *Metall. Trans. A*, 1986, vol. 17A, pp. 2127–37.
- M.E. Fine and J.G. Conley: *Metall. Trans. A*, 1989, vol. 21A, pp. 2609–10.
- 45. S. Chowdhury, K. Sullivan, N. Piekiel, L. Zhou, and M.R. Zachariah: J. Phys. Chem. C, 2010, vol. 114, pp. 9191–95.
- N. Frage, N. Frumin, L. Levin, M. Polak, and M.P. Dariel: *Metall. Mater. Trans. A*, 1998, vol. 29A, pp. 1341–45.
- Z.W. Liu, Q. Han, and J.G. Li: Metall. Mater. Trans. A, 2012, vol. 43A, pp. 4460-63.
- V.T. Witusiewicz, B. Hallstedt, A.A. Bondar, U. Hecht, S.V. Sleptsov, and T.Y. Velikanova: *J. Alloys Compd.*, 2015, vol. 623, pp. 480–96.
- 49. U.R. Kattner, J.C. Lin, and Y.A. Chang: *Metall. Trans. A*, 1992, vol. 23A, pp. 2081–90.
- J.F. Hair, Jr., W.C. Black, B.J. Babin, R.E. Anderson: Multivariate Data Analysis, 2014.
- A.A.A. Kuylen and T.M.M. Verhallen: *J. Econ. Psycho.*, 1981, vol. 1, pp. 217–37.
- 52. A. Lawrence, J.M. Rickman, M.P. Harmer, and A.D. Rollett: *Acta Mater.*, 2016, vol. 103, pp. 681–87.
- V. Uurtio, J.M. Monteiro, J. Kandola, J. Shawe-Taylor, D. Fernandez-Reyes, and J. Rousu: *ACM Comput. Surv.*, 2017, vol. 50, pp. 1–33.
- A. Sherry and R.K. Henson: J. Pers. Assess., 2010, vol. 3891, pp. 37–41.
- 55. K.E. Muller: Am. Stat., 1982, vol. 36, pp. 342-54.
- 56. J.M. Rickman, Y. Wang, A.D. Rollett, M.P. Harmer, and C. Compson: *npj Comput. Mater.*, 2017, vol. 3, pp. 1–5.
- 57. R.C. MacCallum, K.F. Widaman, S. Zhang, and S. Hong: *Psychol. Methods*, 1999, vol. 4, pp. 84–99.
- A.K. Chaubey, S. Scudino, N.K. Mukhopadhyay, M.S. Khoshkhoo, B.K. Mishra, and J. Eckert: *J. Alloys Compd.*, 2012, vol. 536, pp. S134–37.
- Z. Wang, M. Song, C. Sun, and Y. He: *Mater. Sci. Eng. A*, 2011, vol. 528, pp. 1131–37.
- J. Chen, C. Bao, Y. Ma, and Z. Chen: J. Alloys Compd., 2017, vol. 695, pp. 162–70.

- 61. B.M. Tyson, R.K. Abu Al-Rub, A. Yazdanbakhsh, and Z. Grasley: *Composites B*, 2011, vol. 42, pp. 1395–1403.
- H. Shimazaki and S. Shinomoto: *J. Comput. Neurosci.*, 2010, vol. 29, pp. 171–82.
- 63. I. González, S. Déjean, P.G.P. Martin, and A. Baccini: *J. Stat. Software*, 2008, vol. 23, pp. 1–14.
- 64. A. Paknia, A. Pramanik, A.R. Dixit, and S. Chattopadhyaya: *J. Mater. Eng. Perform.*, 2016, vol. 25, pp. 4444–59.
- 65. L. Banks-Sills, V. Leiderman, and D. Fang: *Composites B*, 1997, vol. 28, pp. 465–81.
- V.A. Romanova, R.R. Balokhonov, and S. Schmauder: Acta Mater., 2009, vol. 57, pp. 97–107.
- 67. S. Jin, P. Shen, D. Zhou, and Q. Jiang: Cryst. Growth Des., 2012, vol. 12, pp. 2814–24.
- S. Jin, P. Shen, Q. Lin, L. Zhan, and Q. Jiang: Cryst. Growth Des., 2010, vol. 10, pp. 1590–97.
- B.-X. Dong, H.-Y. Yang, F. Qiu, Q. Li, S.-L. Shu, B.-Q. Zhang, and Q. Jiang: *Mater. Des.*, 2019, vol. 181, p. 107951.
- D. Zhang, H. Liu, L. Sun, F. Bai, Y. Wang, and J. Wang: Crystals, 2017, vol. 7, pp. 1–12.
- L. Arnberg, L. Bäckerud, and H. Klang: *Met. Technol.*, 1982, vol. 9, pp. 7–13.
- D.H. St. John and L.M. Hogan: J. Cryst. Growth, 1979, vol. 46, pp. 387–98.
- 73. M.S. Lee and B.S. Terry: *Mater. Sci. Tech.*, 1991, vol. 7, pp. 608–12.
- 74. V. Auradi and S.A. Kori: *J. Alloys Compd.*, 2008, vol. 453,
- pp. 147–56.75. J. Zhao, T. Wang, J. Chen, L. Fu, and J. He: *Materials*, 2017,
- vol. 10, pp. 1–10. 76. E.G. Kandalova, V.I. Nikitin, J. Wanqi, and A.G. Makarenko:
- Matt. Lett., 2002, vol. 54, pp. 131–34.
 77. Z. Liu, M. Rakita, X. Wang, W. Xu, and Q. Han: J. Mater. Res.,
- 2014, vol. 29, pp. 1354–61.
- 78. X. Wang, A. Jha, and R. Brydson: *Mater. Sci. Eng. A*, 2004, vol. 364, pp. 339–45.
- R. Nikbakht and H. Assadi: Acta Mater., 2012, vol. 60, pp. 4041–53.
- B.B. Khina, B. Formanek, and I. Solpan: *Physica B*, 2005, vol. 355, pp. 14–31.
- M. Ge, D.S. Coburn, E. Nazaretski, W. Xu, K. Gofron, H. Xu,
 Z. Yin, and W.-K. Lee: *Appl. Phys. Lett.*, 2018, vol. 113,
 p. 083109.

Publisher's Note Springer Nature remains neutral with regard to jurisdictional claims in published maps and institutional affiliations.